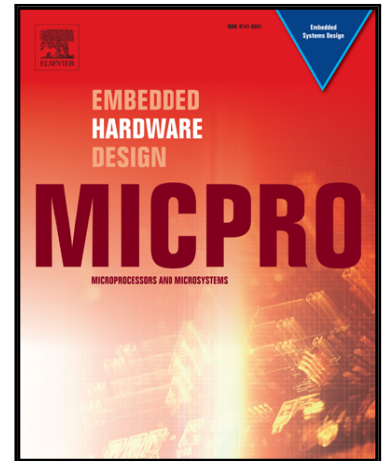


Journal Pre-proof

Performance evaluation of CCOs for the optimization of low-power pressure-based implantable wireless systems

J.A. Miguel , Y. Lechuga , M.A. Allende , M. Martinez

PII: S0141-9331(20)30432-4
DOI: <https://doi.org/10.1016/j.micpro.2020.103273>
Reference: MICPRO 103273



To appear in: *Microprocessors and Microsystems*

Received date: 21 January 2020
Revised date: 23 June 2020
Accepted date: 15 September 2020

Please cite this article as: J.A. Miguel , Y. Lechuga , M.A. Allende , M. Martinez , Performance evaluation of CCOs for the optimization of low-power pressure-based implantable wireless systems, *Microprocessors and Microsystems* (2020), doi: <https://doi.org/10.1016/j.micpro.2020.103273>

This is a PDF file of an article that has undergone enhancements after acceptance, such as the addition of a cover page and metadata, and formatting for readability, but it is not yet the definitive version of record. This version will undergo additional copyediting, typesetting and review before it is published in its final form, but we are providing this version to give early visibility of the article. Please note that, during the production process, errors may be discovered which could affect the content, and all legal disclaimers that apply to the journal pertain.

© 2020 Published by Elsevier B.V.

© 2020. This manuscript version is made available under the CC-BY-NC-ND 4.0 license <http://creativecommons.org/licenses/by-nc-nd/4.0/>

Performance evaluation of CCOs for the optimization of low-power pressure-based implantable wireless systems

J.A. Miguel, Y. Lechuga, M.A. Allende, M. Martinez

Microelectronics Engineering Group (GIM)

Universidad de Cantabria

Avenida Los Castros 46. Edificio ETSIT Departamento TEISA

E-39005 Santander, Cantabria, Spain

Tel: +34 942 201560

Fax: +34 942 201873

{joseangel.miguel, yolanda.lechuga, miguel.angel.allende, mar.martinez}@unican.es

Corresponding Author: Dr. Yolanda Lechuga

yolanda.lechuga@unican.es

yolanda@teisa.unican.es

Title

Performance evaluation of CCOs for the optimization of low-power pressure-based implantable wireless systems.

Abstract

Implantable biomedical devices intended for remote follow-up of Cardiovascular Diseases (CVD) are often based on MEMS pressure sensors and the corresponding CMOS electronics, which are responsible for powering, signal conditioning and data transmission. This kind of heterogeneous systems achieves reduced dimensions and consumption by monolithic integration on the same silicon substrate. The objective of this work is to analyze and fully characterize several Capacitor-Controlled Oscillator (CCO) topologies that can be used for the aforementioned implantable applications, by comparison of their most relevant performance parameters. The results will allow the design optimization of low-power wireless implants, aimed at a future development of embedded systems with real-time data acquisition. Five topologies have been chosen for the evaluation: a standard ring oscillator; a current-starved ring oscillator; a Lee-Kim fully-differential oscillator; a coupled Sawtooth oscillator, and a modified Sawtooth oscillator designed for CCOs biased by a ramped voltage signal. Comprehensive simulations allowed the estimation of the output frequency, percentage tuning range, maximum linearity error, phase noise and power consumption for each design, as well as a Figure of Merit, for every CCO. For the calculation of these performance metrics, the impact of biasing circuits and different tuning strategies has also been considered.

Keywords

Embedded systems; biomedical electronics; implantable biomedical devices; MEMS sensors; capacitance-controlled oscillators.

1. Introduction

From a worldwide perspective, Cardiovascular Diseases (CVD) keep on rating as the first mortality and morbidity cause, in spite of the significant efforts invested in Healthcare for the last decades by developed countries [1]. Besides the 1.8 million CVD-triggered deaths per year (one every 20 seconds), the European Union (EU) must deal with 49 million people who

nowadays are estimated to live with one or several of these chronic conditions [2]. A number that, unfortunately, is expected to rise even more, because of the progressive population aging and the increasing prevalence of major cardiovascular risk factors (hypertension, diabetes, overweight or smoking).

Cardiovascular Implantable Electronic Devices (CIED), used for remote follow-up of CVD, have already proven to be worthwhile to enhance patient's life quality and expectancy, as well as to reduce treatment costs [3, 4], which is beneficial from both people's and Healthcare-systems point of view. On the one hand, these devices are based on secure and innocuous techniques that meet strict clinical requirements. And, on the other hand, they contribute to a more human and closer medicine that empowers CVD patients without jeopardizing their medical condition, and that also improves their quality of life by reducing their frequent attendances to medical consultations and Emergency Rooms (ER).

For that reason, when a patient is diagnosed with a CVD and needs clinic follow-up and decompensation detection, these tasks can be done safely and conveniently by an implantable device that monitors blood pressure remotely. Moreover, the integration of several environmental and body sensors in a future embedded platform with IP-based communication capabilities, will allow to monitor, aggregate and evaluate significant data about the patients' health status in a single health tracker, and also to manually or automatically trigger an emergency call or the submission of real-time measurements to their clinicians [5].

This work focuses on implantable and wireless electronic devices monitoring blood pressure that are based on Micro-Electro-Mechanical Sensors (MEMS) acting as pressure transducers. The electronic circuitry needed for power and data transmission can be monolithically integrated on the same silicon substrate thanks to recent advances on MEMS fabrication techniques that allow full compatibility with CMOS processes. The low-cost and low-power features, as well as the minimized dimensions, of this kind of heterogeneous systems make them suitable candidates for their use as transducers in medical implants.

The low-power requirement permits the use of Wireless Power and Data Transmission (WPDT) techniques to connect the MEMS transducer to an external reader for further evaluation. In this case, the use of capacitive MEMS pressure sensors to acquire blood pressure data is often preferred to their resistive counterparts because of their reduced power consumption.

In order to distinguish and process every remarkable change coming from an implanted capacitive transducer, time or frequency-to-digital conversion is gaining importance when power and area consumptions are strict requirements [6]. In this case, the simpler and most feasible solution entails integrating the capacitive sensors into an oscillator structure, giving rise

to a Capacitive-Controlled Oscillator (CCO) that neither requires extra building blocks nor injects noise to the signal as the Voltage-Controlled Oscillators [7].

To optimize the design of implantable devices to monitor blood pressure for the purpose of CVD follow-up, in this paper different CCO-based topologies with an integrated MEMS capacitor are thoroughly investigated. Section II includes a summary of the previous work developed in the field and Section III provides a description of the CCO architectures selected for a performance comparison. In this section the most relevant performance metrics are explained and a corresponding Figure of Merit (*FOM*) is applied. Section IV presents the simulation results obtained from the previous topologies and the consequent discussion. The paper finishes with Section V, the conclusions.

Journal Pre-proof

2. Previous Work

Three specific CVD conditions (Hypertension (HT), Heart Failure (HF) and Stenosis) have attracted special attention by academia and companies for the development of alternative and non-invasive monitoring techniques with implanted devices, because of their high prevalence and elevated treatment costs.

Hypertension, or High Blood Pressure (HBP), is also known as the “silent killer”, since it can present no symptoms while damaging the heart and blood vessels in organs such as brain and kidneys. Statistics confirm that a 20% of adult population has HBP and half of all deaths caused by stroke and heart disease are related to this illness [1].

The inability of the heart to pump systematically sufficient blood flow to fulfill the demand of the body is a simplified definition of the Heart Failure. HF affects between 2 and 3% of the adults [8] and it is the first cause of hospitalization of people over 65 years old. More specifically, HF is solely responsible for 3% of all hospital admissions. This is one of the reasons why this condition entails a significant economic burden for the healthcare sector [9].

Finally, Stenosis consists of the anomalous narrowing of a blood vessel, often due to an atherosclerotic plaque. When the occlusion affects the coronary arteries, the Percutaneous Coronary Intervention (PCI) procedure with stent implantation is the common treatment for revascularization. A stent is an endoprosthesis based on a biocompatible mesh tube that restores the regular blood-flow in a clogged vessel [10]. However, In-Stent Restenosis (ISR), or the reocclusion of the treated blood vessel by neo-intimal tissue growth, stands out as the main long-term complication of stent implantation [11; 12, 13].

The reasons why these three diseases are more than adequate candidates for the implantation of a pressure sensor for clinical follow-up, apart from their abovementioned high prevalence and treatment costs, are mainly the following: First, reliable and crucial data about the patient's health status can be obtained from pressure measurements, more specifically, from arterial blood pressure (for HT), pulmonary artery or intracardiac pressure (for HF), or intrastent pressure gradient (for ISR). Second, it is possible to take advantage of different endoprosthesis to accommodate the electronic device for implantation, such as the previously mentioned stents, as shown in Fig. 1, or, for example, self-expandable double umbrellas like those used to close the inter-atrial septum of the heart.

Intelligent stents (iStents), or stents with sensing and communication capabilities, have been lately proposed as economic and innocuous alternatives for monitoring ISR [14-23]; although the aforesaid HF condition can also be monitored effectively if the pulmonary artery pressure is

periodically measured by the use of an iStent, as theoretically proposed in [22]. Besides that, the V-LAP™ device, based on a self-expandable double umbrella as anchoring element, has been proposed to measure and transmit left atrial pressure (LAP) for HF follow-up [24].

Regarding existing WPDT techniques, those based on Backscattering schemes, similar to the one described in Fig. 2, imply a promising solution for minimizing power consumption, since the generation of an additional RF signal for the downlink communication is not required, thus preventing the integration of a power-hungry RF oscillator inside the implant [25, 26, 27].

In these schemes the implant antenna is used for both transmitting and receiving RF signals, and it is connected through its port to an Integrated Circuit (IC) with controllable input impedance. If the antenna and chip impedances are perfectly matched ($Z_{ANT} = Z_{IC}^* = Z_{ABS}^*$), all the power available at the antenna can be theoretically fed to the circuit. On the other hand, by appropriate selection of the IC impedance, the power rate between the backscattered signal and the absorbed one can be adjusted ($Z_{ANT} \neq Z_{IC}^*$). Hence, the downlink is obtained by forcing enough changes in the chip impedance. The simpler implementation of a controllable impedance matching circuit comprises a single shunt transistor, located at the input of the IC. Ideally, by periodically switching the transistor between its on and off states, the matching between the antenna and the IC can be drastically changed, varying from a totally-absorbed power operation state (reflection coefficient, $|\rho_{IC}| = 0$) to a fully-reflected power operation state ($|\rho_{IC}| = 1$), resulting in an effective modulation of the backscattered power.

In the particular case of capacitive MEMS pressure sensors, when a backscattering WPDT scheme is used, every remarkable change in the transducers must be distinguished by the amount of power reflected by the implant antenna. Hence, the Capacitive-Controlled Oscillator (CCO) is used to control the switching frequency of the shunt transistor forming the impedance matching block. By this way, as illustrated in Fig. 2 and Fig. 3, the sensor-collected data modulates the envelope frequency (f_{ENV}) of the backscattered power reaching the external reader.

With respect to the optimization of CCO structures for implantable capacitive sensors, to our knowledge, only [7] have considered the need of an exhaustive comparison of existing topologies, based on key parameters, to facilitate the design of these systems, while maximizing their performance. However, this preliminary study did not take into account all the possible topologies, the impact of biasing circuits, or different tuning strategies.

3. Oscillator Topologies and Performance Metrics

3.1. Oscillation Frequency

To perform a fair comparison between the CCO topologies under observation, identical design constraints must be imposed to each design. In this way, a free-running frequency of $f_{OSC} = 435$ kHz has been selected as the initial and most relevant design requirement to be met.

The Industrial, Scientific and Medical (ISM) band centered at $f_C = 433.92$ MHz, also known as LPD433 [28, 29, 30], has been chosen to carry out the backscattering-based WPDT between the implant and the external reader. As seen in Fig. 3, the use of the double sideband amplitude modulation scheme suggested for coding the data to be transmitted limits the oscillator frequency to a maximum of $f_{MAX} = 870$ kHz. In order to ensure that each CCO operates between the band limits, a free-running frequency constraint of $f_{OSC} = 435$ kHz has been enforced, while allowing an ideal oscillator tuning range of 435 kHz. In practice, oscillators present lower tuning ranges due to topology limitations, which lead to a significant unused portion of the spectrum. However, the allocation of the nominal frequency at the center of the 870 kHz sideband guarantees the in-band operation for each device, even assuming the effect of the fabrication process spread.

Alternatively, the ultra-low power Medical Implant Communications Service (MICS) band has been considered to perform the WPDT between the implant and the off-body reader. Nevertheless, the stronger restrictions in the allowed radiated power, together with the potential presence of interfering signals from other implantable devices operating in the same band (pacemakers, defibrillators, etc.) discouraged its usage [31].

3.2. Performance Metrics and Figure of Merit

A reliable comparison between the CCO topologies under observation requires the evaluation of each oscillator's most relevant performance parameters; while also considering the target system functionality and operating conditions. Firstly, the CCO's Power Consumption is the most critical performance parameter to be considered. An excessive power consumption can jeopardize the oscillator compatibility with wirelessly powered implantable electronic devices, where the available power is limited to a few dozens of microwatts. Secondly, each CCO's Percentage Tuning Range (*PTR*), defined as its absolute tuning range ($f_{MAX} - f_{MIN}$) normalized by its free-running frequency (f_{OSC}), is a relevant parameter quantifying the oscillator sensitivity to changes in the sensing capacitor (C_S). An increased *PTR* entails a higher dynamic

range output, together with an enhanced resolution of the sensor-to-digital conversion operated by the external reader. Thirdly, the Phase Noise (denoted as PN or $L\{\Delta f\}$) is the last performance metric taken into account in the calculation of each topology's Figure of Merit (FOM). Oscillators showing elevated PN values, or significant jitter in the time-domain, present a limited accuracy in the CCO period that degrades the precision of the time-to-digital conversion, required to determine the pressure measurements from the MEMS capacitive sensor.

In conclusion, the Power Consumption (P), the Percentage Tuning Range (PTR) and the Phase Noise (PN) are the performance parameters selected to characterize each CCO performance. Thus, the resulting Figure of Merit (FOM), as introduced in [32], is defined as:

$$FOM = 10 \cdot \log \left[\frac{k \cdot T}{P} \cdot \left(\frac{f_{OSC}}{\Delta f} \right)^2 \cdot \left(\frac{PTR}{100} \right)^2 \cdot \frac{1}{L\{\Delta f\}} \right] \quad (1)$$

Where the Phase Noise is normalized to $k \cdot T/P$, k being the Boltzmann constant and T the operation temperature in Kelvin and noting that PN is proportional to the square of the free-running frequency (f_{OSC}) and inversely proportional to the square of the offset frequency from the carrier (Δf) where PN has been measured, and also inversely proportional to the dissipated power (P). The calculated FOM , referred as Power-to-Frequency Normalized (PFN) in [32], provides a unitless number (usually expressed in dB) where the three parameters have the same weight. Besides, these performance metrics have been normalized to allow a fair comparison of different topologies by avoiding any dependency of a particular design criteria. As anticipated, a greater FOM value corresponds to better CCO performance.

In addition to the performance metrics included in the FOM expression, two extra parameters have been evaluated due to their relevance for the proposed application. Firstly, the frequency-to-sensor response (f_{OSC} vs. C_S) for each CCO has been simulated, and the resulting data has been used to estimate its linearity error. By definition, the linearity error is expressed as the maximum deviation of the oscillator response from the best-fit straight line obtained by Least Squares Regression. To equitably compare the linearity between the different CCO topologies, the linearity error has been addressed as a percent of the oscillator Full-Range Output, denoted as the Maximum Linearity Error (MLE) percentage. A strongly linear CCO is advisable as it eases the calibration of the capacitive pressure sensor both before the device implantation and during its useful lifetime.

Lastly, the Frequency Pushing, defined as the CCO output frequency sensitivity to changes in the bias voltage ($S_{V_{DD}}^{f_{OSC}}$), is the second parameter under observation not included in the FOM .

Generally, the biasing of wirelessly powered implantable devices relies on the rectification of an incident RF signal. Different issues can alter the amount of RF power reaching the implant, including the presence of interfering signals and changes in the distance and/or alignment between the device and the off-body emitter. This means that the implanted CCO must operate under variable biasing conditions, while guaranteeing a stable output frequency, thus making bias-insensitive CCOs more desirable for these applications.

3.3. General Oscillator Topologies

The CCOs included in this paper have been designed in TSMC 0.18 μ m CMOS technology, biased by a DC voltage of $V_{DD} = 1.8$ V; and their performance metrics have been obtained from schematic-level simulations performed in Cadence Virtuoso IC6.1.7-64b.500.4.

An initial comparison between CCO topologies is carried out by characterizing the performance of four oscillators: (a) a standard ring oscillator; (b) a current-starved ring oscillator; (c) a Lee-Kim fully-differential oscillator [33]; (d) a coupled Sawtooth oscillator. The schematic view of each CCO stage has been included in Fig. 4. The oscillators have been designed to present a free-running frequency of $f_{OSC} = 435$ kHz and to contain an identical number of individual stages if possible. On this matter, as indicated in Fig. 4, every topology under study comprises 7 stages but the Lee-Kim fully-differential oscillator, which fulfills the design constraints using only a maximum of 4 stages.

In every design, the first stage is loaded by a variable capacitor (C_S). This device models the behavior of a capacitive MEMS pressure sensor fabricated in PolyMUMPS technology by MEMSCAP. This sensor has been designed to measure pulmonary artery hypertension, showing a capacitive range of $C_S = [0.6, 1]$ pF [21]. The remaining stages are loaded by equal static capacitors (C_O). The usage of capacitive sensors in every stage has been previously considered in [22], as it greatly improves the oscillator sensitivity and PTR . However, the size of PolyMUMPS MEMS sensors highly exceeds that of the integrated capacitors in TSMC 0.18 μ m technology, limiting the number of sensors that can be included in the CCO without compromising its implantability.

Thus, knowing the sensor range of $C_S = [0.6, 1]$ pF, and in order to characterize the influence of the loading symmetry on the oscillator performance, several loading conditions ($C_O = 0.6$ pF, 0.7 pF, 0.8 pF, 0.9 pF, 1.0 pF) have been applied to each CCO topology. Since a free-running frequency of $f_{OSC} = 435$ kHz must be kept regardless the static loading conditions, a

total of 20 different oscillator designs have been completed, as depicted in Table 1; each of them requiring different transistor sizing and bias currents.

3.4. Modified Sawtooth Oscillator Topology

Sawtooth relaxation oscillators have extensively proven their reliable operation as CCOs, while presenting promising advantages over ring and differential oscillators, particularly restrained power requirements and wide frequency tuning capabilities through an externally applied voltage signal. Thus, as analytically modeled by equation (2), a Sawtooth oscillator with N stages generates an output signal whose period (T_{OSC}) is proportional to the sensor capacitance and the voltage reference signal.

$$T_{OSC} = \frac{V_{REF}}{I_{BIAS}} \cdot [C_S + (N - 1) \cdot C_O] \quad (2)$$

Where V_{REF} is the DC voltage reference signal used to tune the oscillation frequency, I_{BIAS} is the bias current demanded by each oscillator stage, C_S models the response of a capacitive MEMS pressure sensor loading the first stage, and C_O represents the static loading of the remaining stages.

Despite the aforementioned benefits of Sawtooth CCOs, recent reports have demonstrated the problem of these topologies to achieve a stable oscillation while being biased by a ramped voltage signal. This is an important issue, potentially preventing the inclusion of Sawtooth CCOs in wirelessly powered implantable systems, where the bias voltage V_{DD} is rectified from a RF signal, showing a non-despicable rectifying time before reaching a stable DC value. Although all the simulations presented in this study have been carried out under a constant bias condition of $V_{DD} = 1.8$ V, the analysis of a proposed Sawtooth topology, presented in Fig. 5, has been considered significant enough to be included in this work. As can be observed in the figure, this modified implementation of a Sawtooth oscillator presents slight variations over the regular topology, while being able to reach a sustainable oscillation under ramped biasing conditions, without degrading the CCO performance. The only notable drawback of the modified Sawtooth lies in the larger silicon area needed for its fabrication, due to the increased size of the M_{02A} and M_{02B} transistors [22].

Therefore, a second CCO comparison has been included in the next section, involving the characterization of both the regular Sawtooth oscillator and the proposed modified version. In this case, a total of 12 designs have been compared, as described in Table 2. First, both Sawtooth implementations have been resized in order to present a constant free-running

frequency of $f_{OSC} = 435$ kHz under the different loading (C_O) conditions considered. Second, these CCOs have been tuned by their reference voltage V_{REF} to keep a fixed $f_{OSC} = 435$ kHz, without the need of resizing any of their building components.

Journal Pre-proof

4. Simulation Results and Discussion

4.1. General Oscillator Topologies

In this section the performance results of a set of selected designs are obtained by simulation and presented. This comparison considers: standard ring oscillators, starved-ring oscillators, Lee-Kim fully-differential oscillators and regular Sawtooth oscillators. Every design has been optimized to present a free-running frequency of $f_{osc} = 435$ kHz, for static loading values of $C_O = [0.6, 0.7, 0.8, 0.9, 1.0]$ pF. Thus, a group of 4 CCO topologies, with 5 different loading conditions, leads to a total of 20 oscillator designs.

To prove the accuracy of these designs, Fig. 6 displays the statistical data collected for each topology, regarding its free-running frequency for a nominal sensor value of $C_S = 0.6$ pF and 5 different static loads. The data presented includes the f_{osc} mean values, its 25th and 75th percentiles, as well as its maximum and minimum values. As can be noted, all the designs keep their f_{osc} between 434.35 kHz and 435.90 kHz, reasonably meeting the requirement of $f_{osc} = 435$ kHz, while entailing a maximum relative error of 0.21%.

Additionally, a Kruskal-Wallis [34] test for nonparametric data has been carried out to compare the free-running frequency results for the 4 CCO topologies. The test produces a p-value of $p = 0.8481$, which validates the null hypothesis that the frequency samples for each CCO topology belong to a different population with the same distribution. Thus, this analysis proves that the 4 oscillator topologies have been properly designed to present a nominal output frequency of $f_{osc} = 435$ kHz. As can be noticed in Fig. 6, each topology has been re-designed to keep a constant f_{osc} for the different C_O loading conditions considered. It results in a total of 5 design iterations for each topology, showing f_{osc} deviations around the target 435 kHz value. In this regard, the Kruskal-Wallis test demonstrates that the 4 CCO topologies present a similar distribution for the simulated f_{osc} values.

The capacitance-to-frequency conversion response exhibited by each topology is a performance parameter of interest, given its correlation with the oscillator sensitivity to sensor changes ($S_{C_S}^{f_{osc}}$) and its resultant PTR. Fig. 7 shows the output frequency range simulated for every topology loaded by a capacitance of $C_O = 0.6$ pF, while varying the sensing capacitor in the range of $C_S = [0.6, 1]$ pF. As perceived in the figure, the fully-differential oscillator exhibits the higher sensor sensitivity, compared to the non-differential topologies. This behavior can be explained by looking at the number of stages comprising each CCO. As previously mentioned, the fully-differential oscillator requires a maximum of 4 stages to achieve the design constraints,

thus showing a sensor-to-load ratio of 1/3. On the contrary, the remaining oscillators demand a minimum of 7 stages to fulfill the design constraints, while warranting viable transistor sizing; which reduces the sensor-to-load ratio to only 1/6. For this reason, the fully-differential CCO showcases significantly improved capacitance-to-frequency conversion, reaching an ideal maximum value of twice that obtained for the rest of the topologies.

Similarly, the same behavior can be seen from Fig. 8, which includes the Percentage Tuning Range (*PTR*) results for each design. As expected, the fully-differential CCO provides the maximum *PTR*, while the remaining topologies present comparable results. Another relevant outcome obtained from the inspection of Fig. 8 lies in the *PTR* increase with the loading symmetry. The study of the analytical expressions modeling the oscillation period (T_{OSC}) of ring-based and Sawtooth CCOs helps to explain this behavior. Therefore, equations (2) and (3) can be used to calculate the frequency conversion sensitivity for each CCO, making it possible to correlate their analytical response with the simulations results in Fig. 8. More concretely, equation (3) models the oscillation response of a ring-based CCO built from N stages, where the first stage is loaded with a capacitive MEMS sensor (C_S), while the rest of the stages present equal static loads (C_O) at their outputs.

$$T_{OSC} = 2 \cdot [\tau_S + (N - 1) \cdot \tau_O] \quad (3)$$

Where variables τ_S and τ_O are the average rise and fall time-delays for the C_S -loaded and the C_O -loaded stages, respectively.

Considering identical biasing conditions for each stage of the ring-based CCOs, as well as an output swing limited only by the bias voltage V_{DD} , it is possible to consider the following approximations: $\tau_S = R_{EQ} \cdot C_S$ and $\tau_O = R_{EQ} \cdot C_O$; where R_{EQ} is the equivalent loading resistance, reasonably approximated as $R_{EQ} \cong V_{DD}/I_{BIAS}$. Now, equation (3) can be rewritten as function of the loading capacitors:

$$T_{OSC} = 2 \cdot R_{EQ} \cdot [C_S + (N - 1) \cdot C_O] \quad (4)$$

Finally, from equations (2) and (4) it is feasible to calculate the sensitivity for both ring-based (5) and Sawtooth oscillators (6):

$$S_{C_S}^{f_{OSC}} = \frac{\Delta f_{OSC}}{\Delta C_S} = \frac{1}{2} \cdot \frac{I_{BIAS}}{V_{DD}} \cdot \frac{1}{[C_S + (N - 1) \cdot C_O]} \quad (5)$$

$$S_{C_S}^{f_{osc}} = \frac{\Delta f_{osc}}{\Delta C_S} = \frac{I_{BIAS}}{V_{REF}} \cdot \frac{1}{[C_S + (N-1) \cdot C_O]} \quad (6)$$

Thus, analytical expressions (5) and (6) state that ring-based and Sawtooth CCOs present higher capacitance-to-frequency conversion sensitivity for lower C_O loading values. This behavior matches the simulation results exposed in Fig. 8, proving that symmetrically loaded CCOs, with low-value capacitors, produce better sensitivity and PTR results.

The CCO linearity, displayed in Fig. 9 as the Maximum Linearity Error (MLE) percentage simulated for each topology, is an interesting performance parameter for the goal CCO application, but not included formally in the FOM expression. Oscillators showing low MLE values imply easier calibration of the devices pre and post-implantation, as they present highly linear capacitance-to-frequency behavior. According to the results in Fig. 9, current-starved ring topologies and fully-differential topologies are moderately more linear than the rest, which makes them easier to calibrate. Additionally, Fig. 9 highlights that an asymmetrically loading of the CCOs yields to a more linear frequency vs. sensor capacitance performance, while it worsens the resulting PTR , revealing a first design trade-off.

Regarding the Phase Noise (PN) outcome, single-ended oscillators are expected to produce better results than their differential counterparts [7]. This behavior can be noticed in Fig. 10, where the simulated PN values at 100 kHz away from the carrier are included. Besides, it must be noted that the current-starved ring, the fully-differential and the Sawtooth oscillators, all include a simple current mirror, as the one shown in Fig. 5, for biasing purposes. As reported in the literature [35], the addition of the simpler current mirror implementation to a ring oscillator results in a significant degradation of its PN close to the carrier; particularly when compared to a passive biasing approach. This influence of the current mirror on the PN is easily noticeable by comparing the PN curves for the standard ring and current-starved ring oscillators in Fig. 10, reminding that the former does not comprise an additional biasing block. Concerning the loading symmetry effect on the PN , the simulation results tend to improve as the value of C_O increases and also does the asymmetrical loading. It is noteworthy to remind that all the CCOs compared in Fig. 10 have been resized for each value of C_O ; requiring an increase in their bias current I_{BIAS} to compensate the f_{osc} reduction caused by the increment in the loading capacitors. This compensation is generally achieved by raising the size of their building transistors, which has been proved to enhance the PN performance of CCOs [36], as can be observed in the simulation results shown in Fig. 10.

The power consumption (P) is the most critical performance metric compromising a CCO usability as part of an implantable device. To ensure that every oscillator keeps its power

consumption below a reasonable value of a few dozens of microwatts, the CCOs operation has been simulated under different loading conditions, with a constant sensor value of $C_S = 0.6$ pF; and the resulting dissipated power has been included in Fig. 11. As noticed in the figure, the fully-differential CCO presents a substantially higher power consumption than the remaining oscillators. This behavior is related to the lower number of building stages ($N = 4$) of the differential CCO, which implies the need of higher bias currents for each stage to achieve the target f_{OSC} , significantly augmenting the power dissipated by the oscillator. With respect to the static loading conditions, it can be seen in Fig. 11 that larger C_O values produce power-hungrier oscillators, since their bias currents I_{BIAS} must be increased to counterbalance the effect of larger loads, while maintaining a free-running oscillation of $f_{OSC} = 435$ kHz.

The last performance parameter analyzed, but not included in the *FOM* expression, is the Frequency Pushing; used to measure the output frequency drift due to fluctuations on the bias voltage. Traditionally, differential topologies have proved their superior robustness against substrate and supply noises compared to the single-ended ones [37]. These noise sources present a strong correlation, so fluctuations on the substrate and supply voltages produce similar perturbations on the nodes of the oscillator. The high common mode rejection ratio of differential architectures takes advantage of this effect, reducing the impact of supply and substrate noises on the output frequency. Complementary, the addition of a simple current mirror for biasing helps to reduce the CCO sensitivity to changes in its bias voltage. This theoretical reasoning is supported by the simulation results included in Fig. 12, where it can be observed that the fully-differential CCO, followed by Sawtooth and current-starved ring CCOs, produces the least sensitive output to perturbations in the supply voltage ($V_{DD} = 1.8 \pm 25\%$).

To conclude, the *FOM* for each topology has been plotted in Fig. 13, as well as included together with the simulated performance parameters in Table 3. As appreciated in the figure, the symmetrical loading of the CCOs increases the *FOM* values in most cases, making this design choice preferable for improved oscillator performance. Besides, single-ended ring oscillators present the absolute best *FOM* values, particularly due to their better phase noise performance and lower power consumption. However, the improved robustness of differential CCOs against substrate and supply noises, together with the tuning possibilities of Sawtooth oscillators, make them preferable for wireless implantable applications, where a constant rectified bias voltage is not guaranteed, and the calibration of the sensors is mandatory.

4.2. Sawtooth Oscillator Topologies

This subsection focuses on the performance comparison between the regular Sawtooth and the modified Sawtooth topologies, displayed in Fig. 4d and Fig. 5 respectively. The main characteristics of the CCOs under analysis are enumerated in Table 2, where a total of 12 designs are described. In this regard, it has to be noticed that, as stated in expression (2), Sawtooth oscillators exhibit frequency-tuning capabilities through their reference voltage V_{REF} , which makes possible to maintain a free-running frequency of $f_{OSC} = 435$ kHz under different loading conditions (C_O) without the need of resizing any of their building transistors. The potential benefits of this voltage-based tuning response include an easy adjustment of the output frequency after fabrication, correcting deviations in f_{OSC} caused by the manufacturing process spread; together with the compensation of the f_{OSC} drift occurring during the device lifetime due to aging and the interaction with its biological surroundings. It is also necessary to note that the reference voltage V_{REF} is also used to bias the current mirror, as shown in Fig. 5; limiting the number of voltage signals required to tune the oscillator and increasing the f_{OSC} sensitivity to variations in the control signal V_{REF} .

The same set of simulations have been carried out for the aforementioned topologies as for those included in section 4.1, with two main objectives. First, proving that the proposed modified Sawtooth CCO, with respect to the regular one, produces no performance degradation. Second, demonstrating that tuned Sawtooth CCOs ease the achievement of an accurate f_{OSC} , while offering similar performance results as the ones obtained from resized Sawtooth oscillators.

The first set of simulations provide the free-running frequency values for each topology, as shown in Fig. 14. The statistical analysis of the collected data demonstrates that tuned Sawtooth CCOs produce the least dispersed f_{OSC} values, while also highlighting their tuning capabilities requiring small changes in V_{REF} , as plotted in Fig. 15. The simulated data in Fig. 14 also certifies that the free-running frequency constraint has been successfully fulfilled, as all the designs restrain their f_{OSC} values to the range of 434.44 kHz to 435.71 kHz, resulting in a maximum relative error of 0.16%.

The Kruskal-Wallis test performed to the collected f_{osc} data, results on a p-value of $p = 0.135762$, proving that each Sawtooth CCO produces an average free-running frequency close to the target $f_{osc} = 435$ kHz; while the f_{osc} deviations, caused by the design rearrangements required to adapt the oscillators to the different static C_O loading conditions, are similarly distributed for the 4 Sawtooth CCOs under study.

A second body of simulations has been performed to calculate the Percentage Tuning Range (PTR) for every Sawtooth-based design, with the resulting curves represented in Fig. 16. In the

case of resized Sawtooth CCOs, the PTR curves present a linear degradation with the load C_O . This response is supported by the modelling expressions (2) and (6), showing that the sensor-to-frequency conversion sensitivity ($S_{C_S}^{f_{OSC}}$) is inversely proportional to the capacitive loading of each stage. According to equation (6), this linear degradation of the PTR is expected if the I_{BIAS}/V_{REF} ratio remains unchanged for each design, or if its changes are small compared to those in the load C_O ; which is the case for resized Sawtooth oscillators with constant V_{REF} . On the contrary, tuned Sawtooth CCOs require from variations in their I_{BIAS}/V_{REF} relationship to maintain a fixed free-running f_{OSC} , which deviates their PTR vs. C_O response from the linear behavior obtained for their resized counterparts. However, the inspection of the curves displayed in Fig. 16 indicates that tuned Sawtooth oscillators are slightly more sensitive to changes in the sensor C_S , specifically providing improved PTR values for asymmetrical loading conditions.

In addition, a similar trend can be observed in the Maximum Linearity Error (MLE) percentage curves included in Fig. 17. As anticipated by equations (2) and (6), resized Sawtooth CCOs produce better sensor-to-frequency conversion linearity, which reflects in lower MLE values. These results give rise to a new design trade-off, as linear oscillators are preferred due to their ease of calibration; and superior PTR CCOs show improved sensitivity to sensor variations, which reflects in higher resolution of the digital conversion performed by the off-body reader. On the other hand, tuned Sawtooth CCOs present worse PTR and MLE figures, but their tuning capabilities provide robustness against undesired f_{OSC} deviations.

The main source of Phase Noise (PN) in CCOs are the flicker and thermal noises from MOS transistors [38]. Particularly, PN close to the output frequency f_{OSC} is dominated by flicker noise, and its contribution can be reduced by increasing the transistor area (WL) and/or decreasing the device transconductance (g_m), as demonstrated analytically in [36]. This theoretical behavior correlates with the PN results included in Fig. 18, where modified Sawtooth oscillators present superior PN values. It has been reported that the proposed modifications applied to the Sawtooth topology do not degrade the original CCO performance, with the only drawback being the increase of transistors M_{02A} and M_{02B} areas [22]. Thus, in terms of PN , this transistor size increment for modified Sawtooth oscillators translates into a flicker noise reduction and improved PN performance. Furthermore, an identical tendency is observed for the resized Sawtooth CCOs regarding their PN values. An oscillator with a larger loading capacitor C_O will require a higher I_{BIAS} current to generate an equal free-running frequency (f_{OSC}). This increment in the bias current is achieved by augmenting the transistors' aspect ratios (W/L). Hence, more asymmetrically loaded Sawtooth oscillators present larger

MOS devices, effectively reducing their flicker noise contribution and decreasing the resulting PN figures, as appreciated in Fig. 18.

The Power (P) consumption requirements for the designed Sawtooth oscillators are displayed in Fig. 19. On one hand, the plotted curves indicate that the modified Sawtooth topologies increase the power consumption, but showing a moderate increment of 5.6% with respect to the consumption from regular Sawtooth implementations. On the other hand, the change in the loading conditions significantly affect the power demands from each Sawtooth oscillator; as higher bias currents are needed to keep a constant f_{OSC} for larger C_O capacitors. This I_{BIAS} current increase, needed for both the resized and the tuned Sawtooth CCOs, is achieved by raising the aspect ratio of the building transistors, or by augmenting the current flowing through the mirror by increments in the reference input V_{REF} , respectively. For this reason, both Sawtooth implementations present a similar trend in Fig. 19, which makes preferable the use of symmetrically loaded CCOs for low-power applications.

A detailed comparison between each Sawtooth oscillator, regarding their f_{OSC} sensitivity to changes in the biasing voltage, is shown in Fig. 20. It is noticeable that the C_O loading conditions impact the oscillator sensitivity, as analytically expressed in:

$$S_{V_{DD}}^{f_{OSC}} = \frac{\Delta I_{BIAS}}{\Delta V_{DD}} \cdot \frac{1}{V_{REF}} \cdot \frac{1}{[C_S + (N - 1) \cdot C_O]} \quad (7)$$

Moreover, considering all MOSFETs operating in the strong inversion region, it can be stated that the bias current is proportional to the square of the bias voltage. This quadratic relationship makes the term $\Delta I_{BIAS}/\Delta V_{DD}$ dominate over C_O changes in equation (7), as can be observed in Fig. 20. Therefore, Frequency Pushing results show that symmetrically loaded Sawtooth CCOs are less sensitive to noise in their bias voltage, making this configuration particularly interesting for wireless powered applications. Besides, Fig. 20 exposes the robustness of differential architectures against substrate and supply noises [37]. For this reason, the modifications applied to Sawtooth oscillators increase their sensitivity to supply changes, as the new stage topology cannot be considered purely differential.

To sum up, the calculated Figure Of Merit (FOM) for each Sawtooth CCO is presented in both Fig. 21 and Table 4. The first conclusion obtained from the FOM curves is that the modified Sawtooth implementations not only ensure as good performance as the regular ones, but also improve their FOM values. The main contributor to this upgrade is the better phase noise response provided by modified Sawtooth CCOs, due to their reduced flicker noise. Besides that, the general performance for both regular and modified Sawtooth oscillators has been proved to

be quite similar, while the latter guarantee to achieve a sustainable oscillation when biased by a ramped voltage signal.

5. Conclusions

The adequacy of different Capacitor-Controlled Oscillator (CCO) topologies for its use in implantable electronic devices has been evaluated through a comprehensive set of simulations. The most relevant performance parameters have been obtained for each topology under different loading conditions, giving as a result 32 designs built in TSMC 0.18 μm CMOS technology. The simulation results allowed the accurate estimation of the oscillation frequency, percentage tuning range, maximum linearity error, phase noise at 100 kHz from the carrier and power consumption for each design. Some of these performance metrics have been used to obtain the figure of merit for each CCO, proving a better overall response from single-ended ring topologies when symmetrically loaded. However, the robustness of the differential topologies against supply and substrate noises, together with the voltage tuning possibilities of the Sawtooth CCOs, encourages their use within low-power implantable applications, where reliable calibration and supply insensitivity are desirable. Besides, a modified Sawtooth topology, that solve the stability problems of regular Sawtooth CCOs when biased by ramped voltage signals, has been also analyzed in this work. This topology has proved to minimize the required changes on the regular implementation, while not degrading the overall CCO performance. Moreover, the computed figure of merit for the modified Sawtooth oscillator exhibits better values than its regular counterpart, particularly due to its improved phase noise response. Hence, the modified Sawtooth topology guarantees to achieve a stable oscillation when biased by rectified voltage signals while offering an enhanced performance, which makes it perfectly suitable for wirelessly powered implantable applications.

The results obtained in this work represent a significant step towards the implementation of optimized wireless low-power implants, aimed at the future development of embedded systems with real-time acquisition that could monitor and evaluate CVD-patients' health status.

Acknowledgments

This work was carried out in collaboration with the Hospital Marqués de Valdecilla and its medical research institute IDIVAL, in the context of the “Self-Expanding Dual-Anchor Umbrella with Wireless Monitoring Feature of Intra-Atrial Pressure” project (DTS19/00094). Financial support is provided by the Ministerio de Ciencia, Innovación y Universidades

(Spanish Government), by means of its annual call for Technological Development Projects in Health (DTS2019) under the framework of the Health Research and Development Strategy (AES) that, in turn, belongs to the State Plan for Scientific and Technical Research and Innovation 2017-2020, whose objectives are aligned with the ones highlighted by the European Union under Horizon 2020.

Funding Sources

Funding: This work was supported by the the Ministerio de Ciencia, Innovación y Universidades (Spanish Government), State Plan for Scientific and Technical Research and Innovation 2017-2020, project DTS19/00094.

Conflict of interest

None

Journal Pre-proof

References

- [1] Global Health Estimates 2015: Deaths by Cause, Age, Sex, by Country and by Region, 2000-2015. Geneva, World Health Organization; 2016.
- [2] E. Wilkins, L. Wilson, K. Wickramasinghe, P. Bhatnagar, J. Leal, R. Luengo-Fernandez, R. Burns, M. Rayner, N. Townsend, European Cardiovascular Disease Statistics 2017, European Heart Network, Brussels, 2017.
- [3] C.C. Cheung, M.W. Deyell, Remote Monitoring of Cardiac Implantable Electronic Devices, *Canadian Journal of Cardiology*, vol. 34(7), pp. 941-944, 2018.
- [4] J.P. Piccini, S. Mittal, J. Snell, J.B. Prillinger, N. Dalal, N. Varma, Impact of remote monitoring on clinical events and associated health care utilization: A nationwide assessment, *Heart Rhythm*, vol. 13(12), pp. 2279-2286, 2016.
- [5] A. Fanariotis, F. Andriopoulou, T. Orphanoudakis, I. Politis, An embedded framework enabling access of elderly and disabled persons to IP-based emergency communications, *Microprocessors and Microsystems*, vol. 68, pp. 74-83, 2019.
- [6] H. Danneels, F. Piette, V. De Smedt, W. Dehaene and G. Gielen, A Novel, PLL-based Frequency-to-Digital Conversion Mechanism for Sensor Interfaces, *Sensors & Actuators: A. Physical* vol. 172(1), pp 220-227, 2011.
- [7] J. Van Rethy, H. Danneels, K. Coddens, G. Gielen, Capacitance controlled oscillator optimization for integrated capacitive sensors with time/frequency-based conversion, *Proceedings of EUROSENSORS XXV*, September 2011.
- [8] A.P. Maggioni, U. Dahlström, G. Filippatos, et al., Heart Failure Association of the European Society of Cardiology (HFA). 2013. EURObservational Research Programme: regional differences and 1 - year follow - up results of the Heart Failure Pilot Survey (ESC - HF Pilot), *Eur J Heart Fail*, vol. 15(7), pp 808-817, 2013.
- [9] I. Sayago-Silva, F. García-López, J. Segovia-Cubero, Epidemiology of Heart Failure in Spain Over the Last 20 Years, *Rev Esp Cardiol*, vol. 66(8), pp.649-656, 2013.
- [10] P.W. Serruys, B.H. Strauss, H.M. van Beusekom, W.J. van der Giessen, Stenting of coronary arteries: Has a modern pandora's box been opened?, *Journal of the American College of Card*, vol. 17(6), pp. 143-154, 1991.
- [11] R.E. Kuntz, D.S. Baim, Defining coronary restenosis. Newer clinical and angiographic paradigms, *Circulation*, vol. 88(3), pp. 1310-1323, 1993.

- [12] S. Cassese, R.A. Byrne, T. Tada, S. Piniack, M. Joner, T. Ibrahim, L.A. King, M. Fusaro, K-L. Laugwitz, A. Kastrati, Incidence and predictors of restenosis after coronary stenting in 10 004 patients with surveillance angiography, *Heart*, vol. 100(2), pp. 153-159, 2013.
- [13] L. Mauri, T.S. Silbaugh, R.E. Wolf, K. Zelevinsky, A. Lovett, Z. Zhou, F.S. Resnic, S-L.T. Normand, Long-term clinical outcomes after drug-eluting and bare-metal stenting in Massachusetts, *Circulation*, vol. 118(18), pp. 1817-1827, 2008.
- [14] K. Takahata, Y.B. Gianchandani, K.D. Wise, Micromachined antenna stents and cuffs for monitoring intraluminal pressure and flow, *Journal of Microelectromechanical Systems*, vol. 15(5), pp. 1289-1298, 2006.
- [15] E.Y. Chow, A.L. Chlebowski, S. Chakraborty, W.J. Chappell, P.P. Irazoqui, Fully wireless implantable cardiovascular pressure monitor integrated with a medical stent, *IEEE Transactions on Biomedical Engineering*, vol. 57(6), pp. 1487-1496, 2010.
- [16] K. Keikhosravy, A. Zargar-Yazd, S. Mirabbasi, On the use of smart stents for monitoring in-stent restenosis. In 2012 Annual International Conference of the IEEE Engineering in Medicine and Biology Society, pp. 3231-3234, 2012.
- [17] K. Keikhosravy, P. Kamalinejad, L. Keikhosravy, A. Zargar-Yazd, K. Takahata, S. Mirabbasi, A fully integrated telemonitoring system for diagnosing in-stent restenosis. In 2014 IEEE Biomedical Circuits and Systems Conference (BioCAS) Proceedings, pp. 392-395, 2014.
- [18] X. Chen, D. Brox, B. Assadsangabi, Y. Hsiang, K. Takahata, Intelligent telemetric stent for wireless monitoring of intravascular pressure and its in vivo testing, *Biomed Microdevices*, vol. 16(5), pp. 745-759, 2014.
- [19] J. Park, J.-K. Kim, S.J. Patil, J.-K. Park, S. Park, and D.-W.-Lee, A wireless pressure sensor integrated with a biodegradable polymer stent for biomedical applications, *Sensors*, vol. 16(6), 809(1-13), 2016.
- [20] X. Chen, B. Assadsangabi, Y. Hsiang, K. Takahata, Enabling Angioplasty-Ready “Smart” Stents to Detect In-Stent Restenosis and Occlusion, *Adv. Sci. (Weinh)* Feb. 2018, vol. 5(5), pp. 1700560 (1-10), 2018.
- [21] J.A. Miguel, D. Rivas, Y. Lechuga, M.A. Allende, M. Martinez. A novel computer-assisted design tool for implantable MEMS pressure sensors, *Microprocessors and Microsystems*, vol. 46(Part A), pp. 75-83, 2016.
- [22] J.A. Miguel, Smart Stent for Cardiovascular Restenosis Wireless Monitoring, Ph.D dissertation, ETS de Ingenieros Industriales y de Telecomunicación., Universidad de Cantabria, Santander, 2017.

- [23] J.A. Miguel, Y. Lechuga, M. Martinez. AFM-Based Characterization Method of Capacitive MEMS Pressure Sensors for Cardiological Applications. *Micromachines* 2018, vol, 9(7), pp. 342(1-17); 2018.
- [24] L. Perl, E. et al. A Novel Wireless Left Atrial Pressure Monitoring System for Patients with Heart Failure, First Ex-Vivo and Animal Experience. *Journal of Cardiovascular Translational Research* (2 January 2019), pp. 1-9, 2019.
- [25] W. Liu, K. Huang, X. Zhou, S. Durrani, Next generation backscatter communication: systems, techniques, and applications, *EURASIP Journal on Wireless Communications and Networking* (2019), vol. 2019(69), pp. 1-11, 2019.
- [26] K. Keikhosravy, P. Kamalinejad, A. Zargaran-Yazd, S. Mirabbasi, K. Takahata, V.C. Leung, A feasibility study of using backscattering for telemonitoring of in-stent restenosis, In *Proceedings of the 35th Annual International Conference of the IEEE Engineering in Medicine and Biology Society*, vol. 2013, pp. 5167-5170, 2012.
- [27] L. Mayer, *Antenna Design for Future Multi-Standard and Multi-Frequency RFID Systems*, Ph.D. thesis, Vienna University of Technology, 2009.
- [28] D. Paret, J-P. Huon, "Secure Connected Objects". John Wiley & Sons, 2017.
- [29] The European Telecommunications Standards Institute (ETSI). Short Range Devices (SRD) operating in the frequency range 25 MHz to 1 000 MHz; Part 2: Harmonised Standard for access to radio spectrum for non specific radio equipment. ETSI EN 300 220-2 V3.2.1 (2018-06) (<https://www.etsi.org/>)
- [30] Electronic Communications Committee within the European Conference of Postal and Telecommunications (CEPT-ECC). ECC Recommendation 70-03. Relating to the use of Short Range Devices (SRD). Tromsø 1997. Subsequent amendments 12 June 2020. (<https://www.ecodocdb.dk/>)
- [31] R. Liu, Y. X. Guo, S. Q. Xiao, A review of implantable antennas for wireless biomedical devices, *Forum for electromagnetic research methods and application technologies (FERMAT)*, vol. 14(3), pp. 1-11, 2016.
- [32] D. Ham, A. Hajimiri, Concepts and Methods in Optimization of Integrated LC VCOs, *IEEE JSSC*, vol. 36(6), pp. 896-909, 2001
- [33] J. Lee, B. Kim, A low-noise fast-lock phase-locked loop with adaptive bandwidth control, *IEEE J. Solid-State Circuits*, vol. 35(8), pp. 1137-1145, 2000.
- [34] P.H. Kvam, B. Vidakovic, *Nonparametric Statistics with Applications to Science and Engineering*, first ed., John Wiley & Sons, Inc., Hoboken, New Jersey, 2007.

- [35] S. Gagliolo, G. Pruzzo, D. Caviglia, Phase Noise Performances of a Cross-Coupled CMOS VCO with Resistor Tail Biasing, Proceedings of the 18th Annual Symposium on Integrated Circuits and Systems Design, SBCCI 2005, pp. 149-153, 2005.
- [36] A. Jerng, C.G. Sodini, The impact of device type and sizing on phase noise mechanisms, IEEE J. Solid-State Circuits, vol. 40(2), pp. 360-369, 2005.
- [37] A. Hajimiri, S. Limotyrakis, T. Lee, Jitter and phase noise in ring oscillators, IEEE JSSC, vol. 34(6), pp. 790-804, 1999.
- [38] C. Nam et al., Design optimizations of phase noise, power consumption and frequency tuning for VCO, J. Semicond., vol. 34(9), pp. 095009(1-6), 2013.

Journal Pre-proof

Figures

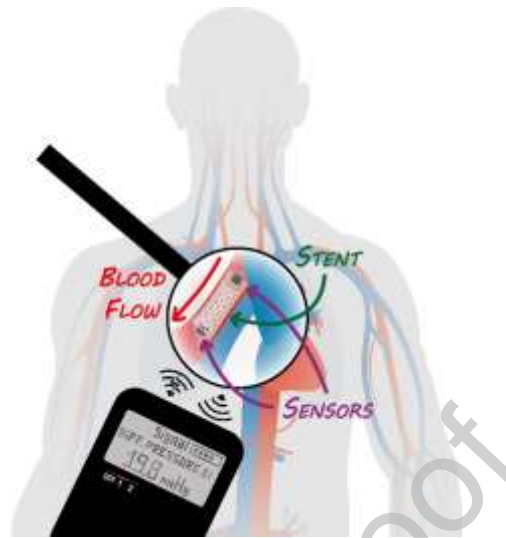


Fig. 1. Concept of a smart stent for In-Stent Restenosis (ISR) wireless monitoring

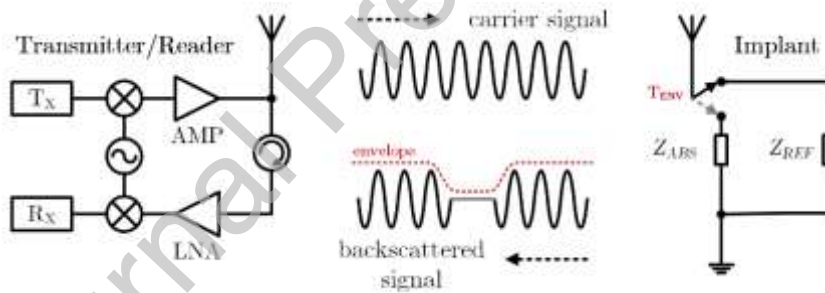


Fig. 2. Architecture of a backscattering-based Wireless Powering and Data Transmission (WPDT) system

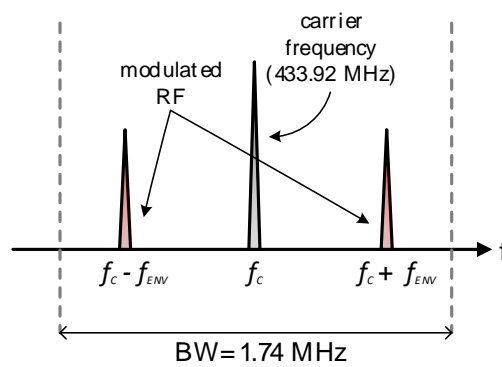


Fig. 3. Spectrum of a backscattering transmission in the LPD433 ISM band

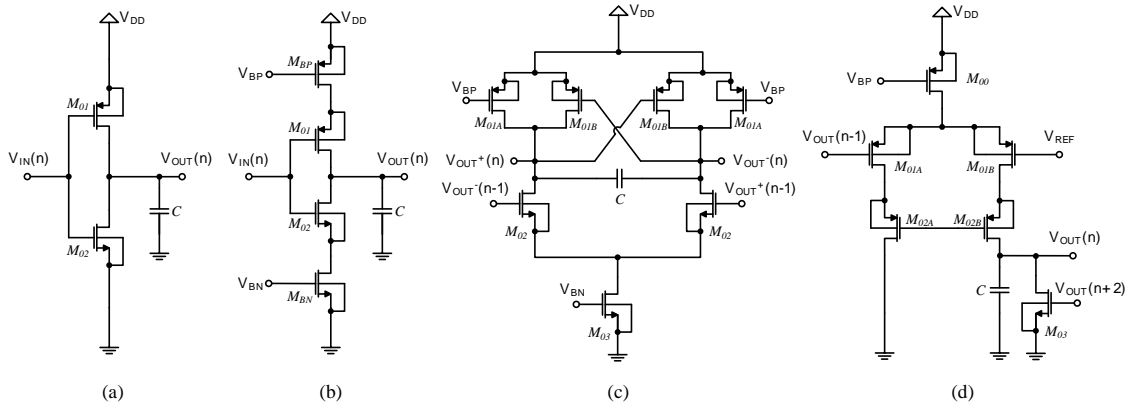


Fig. 4. Single stage schematic views of (a) standard ring oscillator (7-stages); (b) current-starved ring oscillator (7-stages); (c) Lee-Kim fully-differential oscillator (4-stages); (d) coupled-Sawtooth oscillator (7-stages)

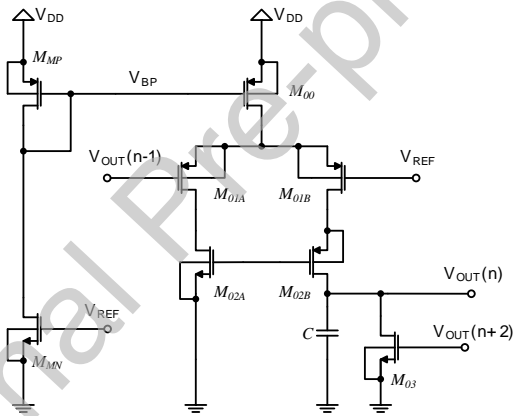


Fig. 5. Single stage schematic view of a modified Sawtooth oscillator, including the biasing current mirror

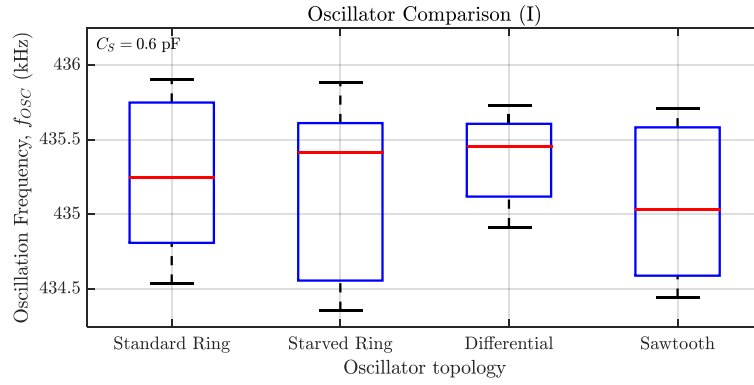


Fig. 6. Statistical analysis of the free-running frequency for each CCO topology, simulated for a common sensor value of $C_S = 0.6$ pF and various loading conditions $C_O = [0.6, 0.7, 0.8, 0.9, 1.0]$ pF

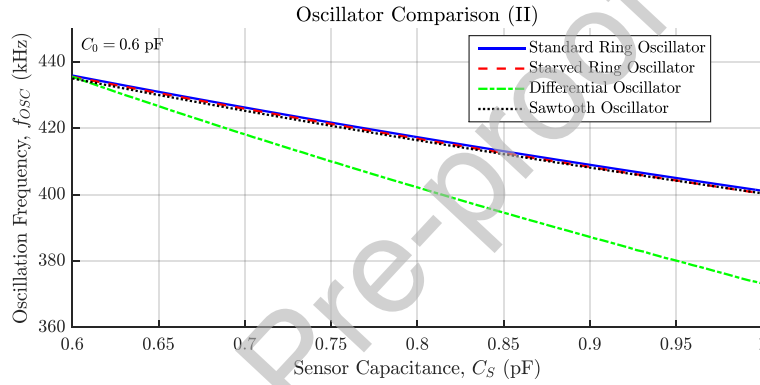


Fig. 7. Frequency (f_{osc}) vs. sensor capacitance (C_S) for each CCO topology, with a static loading of $C_O = 0.6$ pF

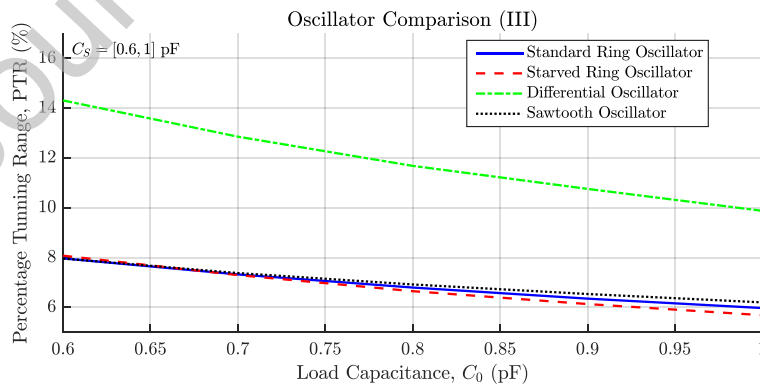


Fig. 8. Percentage Tuning Range (PTR) for each CCO topology, simulated for sensor values in the range $C_S = [0.6, 1]$ pF, and various loading conditions C_O

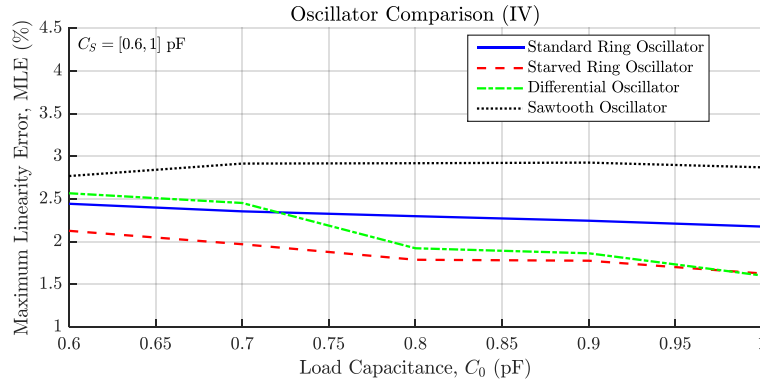


Fig. 9. Maximum Linearity Error percentage (*MLE*) for each CCO topology, simulated for sensor values in the range $C_S = [0.6, 1]$ pF, and various loading conditions C_0

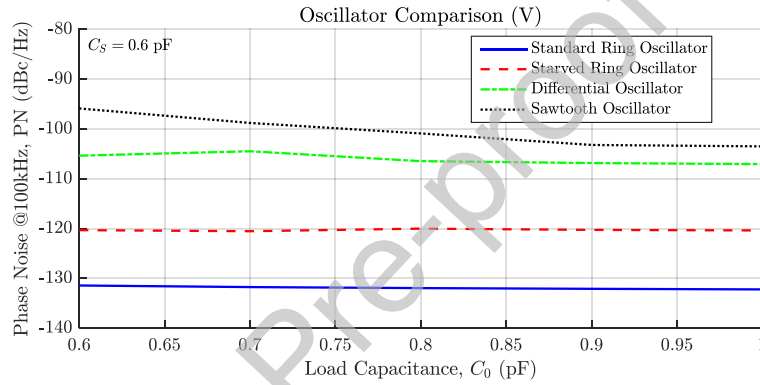


Fig. 10. Phase Noise (*PN*) at 100 kHz away from the carrier, simulated for each CCO topology with a sensor value of $C_S = 0.6$ pF, and various loading conditions C_0

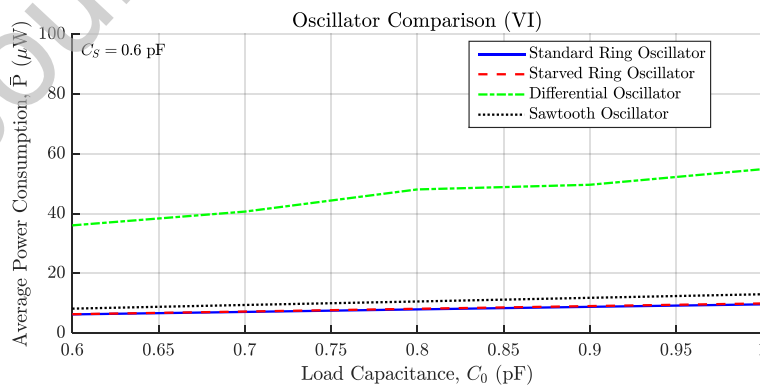


Fig. 11. Average Power consumption (*P*) simulated for each CCO topology with a sensor value of $C_S = 0.6$ pF, and various loading conditions C_0

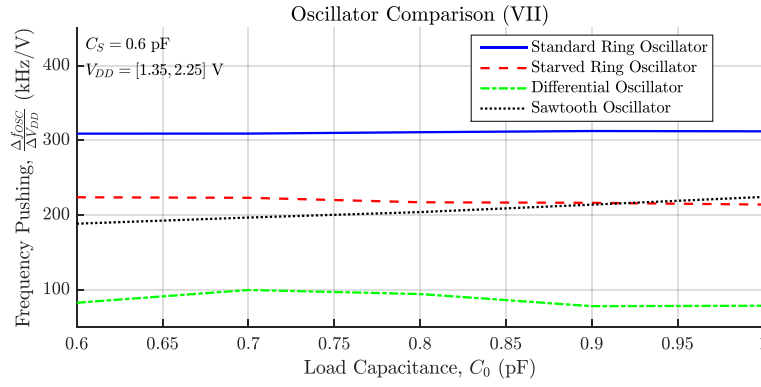


Fig. 12. Frequency Pushing for each CCO topology, simulated with bias voltages between $V_{DD} = [1.35, 2.25]$ V, a sensor value of $C_S = 0.6$ pF, and various loading conditions C_0

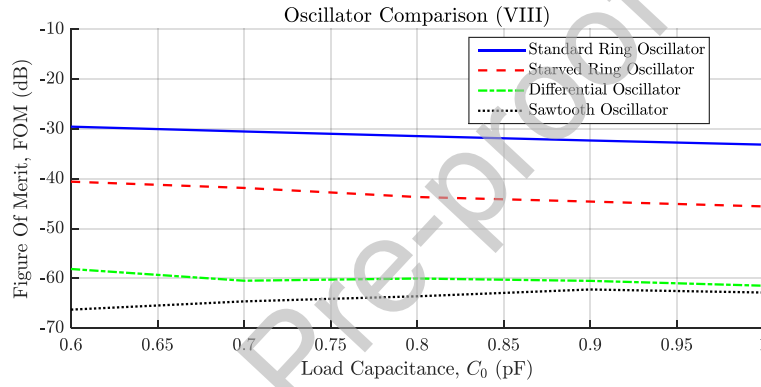


Fig. 13. Resulting Figure Of Merit (FOM) for each CCO topology

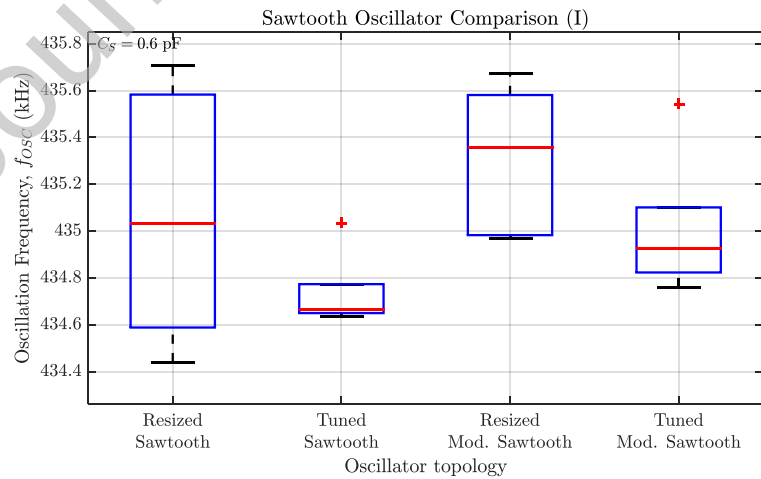


Fig. 14. Statistical analysis of the free-running frequency for each Sawtooth CCO, simulated for a common sensor value of $C_S = 0.6$ pF and various loading conditions $C_0 = [0.6, 0.7, 0.8, 0.9, 1.0]$ pF

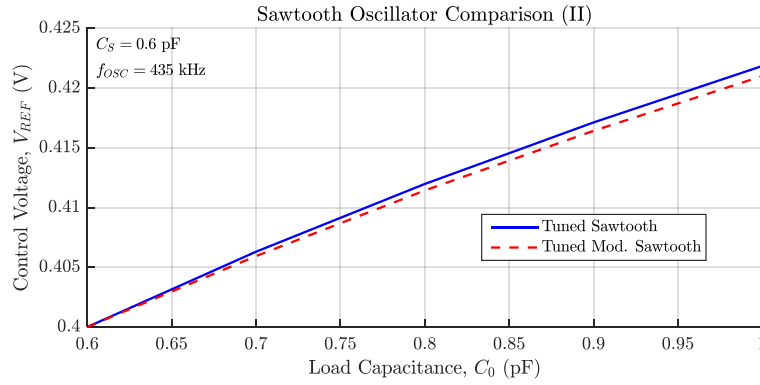


Fig. 15. Control voltage (V_{REF}) vs. load capacitance (C_O) for tuned Sawtooth CCOs, with a sensor value of $C_S = 0.6$ pF, providing a constant $f_{OSC} = 435$ kHz

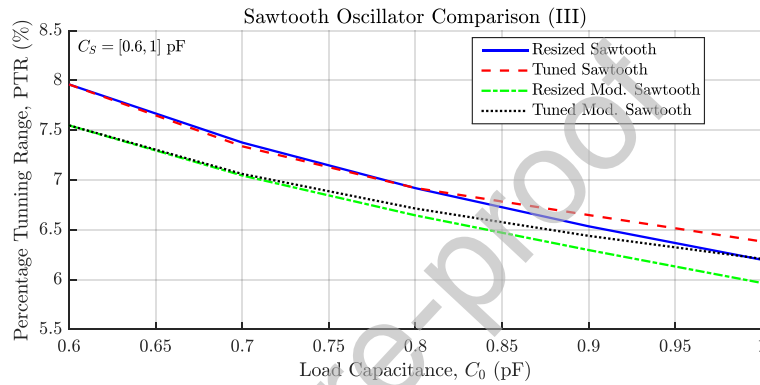


Fig. 16. Percentage Tuning Range (PTR) for each Sawtooth CCO, simulated for sensor values in the range $C_S = [0.6, 1]$ pF, and various loading conditions C_O

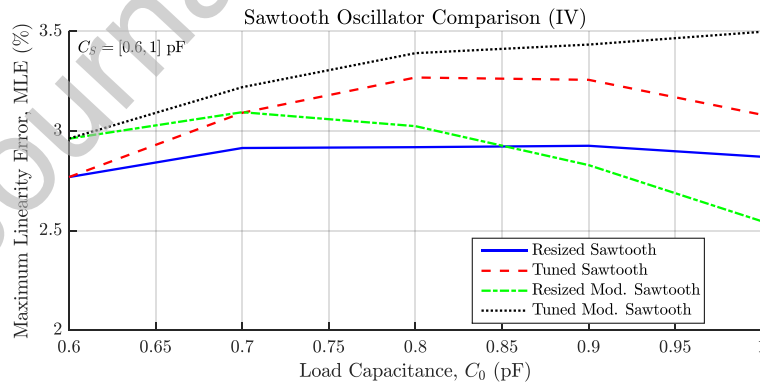


Fig. 17. Maximum Linearity Error percentage (MLE) for each Sawtooth CCO, simulated for sensor values in the range $C_S = [0.6, 1]$ pF, and various loading conditions C_O

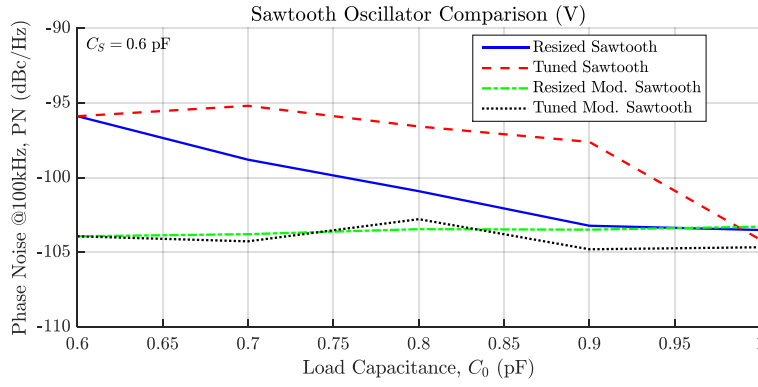


Fig. 18. Phase Noise (PN) at 100 kHz away from the carrier, simulated for each Sawtooth CCO with a sensor value of $C_S = 0.6 \text{ pF}$, and various loading conditions C_0

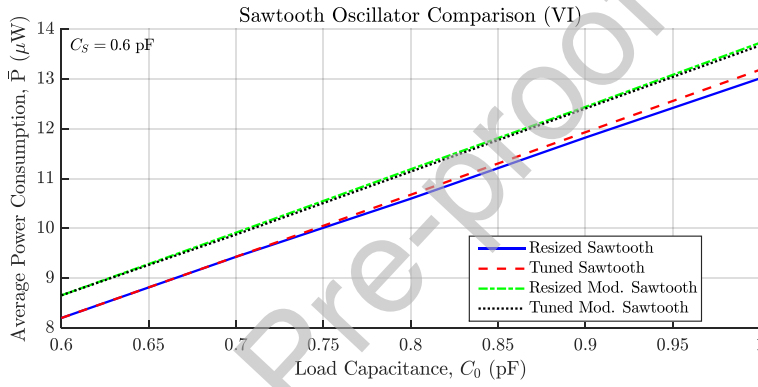


Fig. 19. Average Power consumption (P) simulated for each Sawtooth CCO with a sensor value of $C_S = 0.6 \text{ pF}$, and various loading conditions C_0

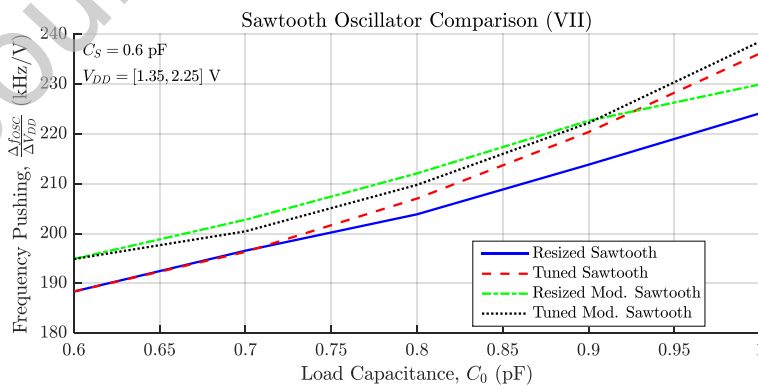


Fig. 20. Frequency Pushing for each Sawtooth CCO, simulated with bias voltages between $V_{DD} = [1.35, 2.25] \text{ V}$, a sensor value of $C_S = 0.6 \text{ pF}$, and various loading conditions C_0

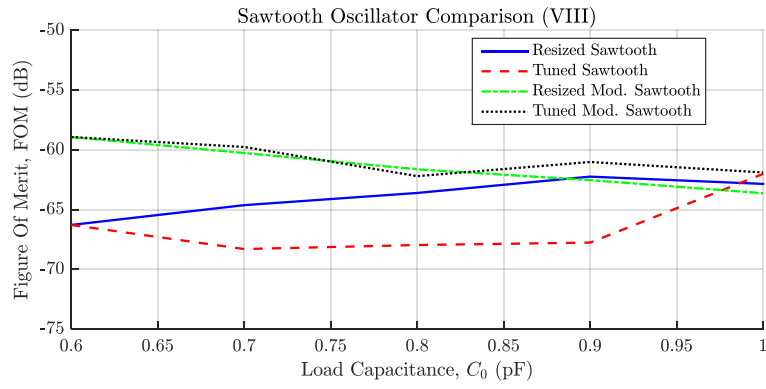


Fig. 21. Resulting Figure Of Merit (FOM) for each Sawtooth CCO

Figure Column Fitting

Figure	Column Fitting
1	1 column
2	1.5 or 2 columns
3	1 column
4	2 columns
5	1 column
6	1 column
7	1 column
8	1 column
9	1 column
10	1 column
11	1 column
12	1 column
13	1 column
14	1 column
15	1 column
16	1 column

Figure	Column Fitting
17	1 column
18	1 column
19	1 column
20	1 column
21	1 column

Journal Pre-proof

Tables

Topology	C_S (pF)	C_O (pF)	Stages (N)	Designs
Ring Oscillator	0.6 – 1.0	0.6	7	5
Starved-Ring Oscillator		0.7	7	5
Lee-Kim Differential Oscillator		0.8	4	5
		0.9	4	5
Sawtooth Oscillator		1.0	7	5

Table 1. Main characteristics and number of design iterations for general CCO topologies

Topology	C_S (pF)	C_O (pF)	V_{REF} (V)	Stages (N)	Designs
Resized Sawtooth Oscillator	0.6 – 1.0	0.6	0.4	7	5
Tuned Sawtooth Oscillator		0.7	0.4 – 0.4218		1
Resized Modified Sawtooth Oscillator		0.8	0.4 V		5
		0.9	0.4 V		5
Tuned Modified Sawtooth Oscillator		1.0	0.4 – 0.4210		1

Table 2. Main characteristics and number of design iterations for Sawtooth-based CCO topologies

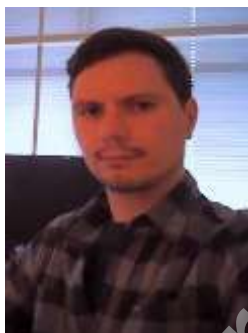
Oscillator	f_{osc} (kHz)	PTR (%)	MLE (%)	PN (dBc/Hz @ 100 kHz)	P (μ W)	FOM (dB)
Standard Ring	435.91	7.96	2.44	-131.44	6.27	-29.55
Starved Ring	435.52	8.07	2.13	-120.33	6.34	-40.59
Fully Diff.	435.57	14.31	2.57	-105.37	36.07	-58.13
Sawtooth	435.03	7.96	2.77	-95.89	8.20	-66.29

Table 3. CCO topologies comparison table for symmetrical loading with $C_O = 0.6$ pF

Oscillator	f_{osc} (kHz)	PTR (%)	MLE (%)	PN (dBc/Hz @100 kHz)	P (μ W)	FOM (dB)
Resized Sawtooth	435.03	7.96	2.77	-95.89	8.20	-66.29
Tuned Sawtooth	435.03	7.96	2.77	-95.89	8.20	-66.29
Resized Mod. Sawtooth	435.55	7.55	2.96	-103.93	8.66	-58.93
Tuned Mod. Sawtooth	435.55	7.55	2.96	-103.93	8.66	-58.93

Table 4. Sawtooth CCOs comparison table for symmetrical loading with $C_o = 0.6$ pF

Authors' Biography



Jose A. Miguel received the B.S., M.S. and PhD. degrees in Telecommunications Engineering from University of Cantabria, Santander, Spain in 2007, 2012 and 2017 respectively. During 2007 and 2010 he was a research fellow in the Communications Engineering Department at the University of Cantabria. He is currently working with the Microelectronics Engineering Group (GIM), in the Electronics Technology, Systems and Automation Engineering Department at the University of Cantabria (Spain). His current research interests include the design and test of heterogeneous systems for biomedical applications.



Yolanda Lechuga received a degree in Industrial Engineering in April 2000. Since then, she has been collaborating with the Microelectronics Engineering Group at the University of Cantabria (Spain), in the Electronics Technology, Systems and Automation Engineering Department. She finished her Ph.D. in 2009 and she has been member of the IEEE since 2002. Nowadays, she is an assistant professor at this university. Her current research area is the design and design-for test of analog, mixed-signal and heterogeneous integrated circuits for biomedical applications, with special emphasis on cardiac implanted devices.



Miguel A. Allende received the graduate and Ph.D. degrees from the University of Cantabria, Santander, Spain, in 1985 and 1994, respectively. In 1996, he became an Assistant Professor of Electronic Technology at the same institution. He was appointed Head of the Department of Electronics Technology, Systems and Automation Engineering in 2014. His main research interest is mixed circuits design and test for industrial applications, and currently, he is engaged in the research and development of heterogeneous systems for implantable medical devices, including the analysis of testable design proposals and test methods.



Mar Martínez received her graduate degree and Ph.D. from the University of Cantabria (Spain) in 1986 and 1990, respectively. She is associate professor of electronic technology at the University of Cantabria (Spain). At present, she is a member of the Electronics Technology, Systems and Automation Engineering Department in the Industrial and Telecommunication Engineering School. She has participated in several EU and Spanish National Research Projects as research and leader. Her main research interest is mixed, analogue and digital circuit testing. She is also interested in the design and test of heterogeneous systems for biomedical applications.